



HAL
open science

Homogenization Based Topology Optimization of Fluid-Pressure Loaded Structures using the Biot-Darcy Model

Godfred Oheneba Agyekum, Laurent Cangémi, François Jouve

► **To cite this version:**

Godfred Oheneba Agyekum, Laurent Cangémi, François Jouve. Homogenization Based Topology Optimization of Fluid-Pressure Loaded Structures using the Biot-Darcy Model. Optimization and Engineering, 2024, 10.1007/s11081-023-09811-1 . hal-04397628

HAL Id: hal-04397628

<https://ifp.hal.science/hal-04397628>

Submitted on 16 Jan 2024

HAL is a multi-disciplinary open access archive for the deposit and dissemination of scientific research documents, whether they are published or not. The documents may come from teaching and research institutions in France or abroad, or from public or private research centers.

L'archive ouverte pluridisciplinaire **HAL**, est destinée au dépôt et à la diffusion de documents scientifiques de niveau recherche, publiés ou non, émanant des établissements d'enseignement et de recherche français ou étrangers, des laboratoires publics ou privés.

Homogenization Based Topology Optimization of Fluid-Pressure Loaded Structures using the Biot-Darcy Model

Godfred Oheneba Agyekum^{1*}, Laurent Cangémi^{1†}
and François Jouve^{2†}

^{1*}IFP Energies nouvelles, Rueil-Malmaison, 92852, France.

²Université Paris Cité, Laboratoire Jacques-Louis Lions (LJLL),
Paris, F-75006, France.

*Corresponding author(s). E-mail(s):

godfred.a.o.ezail@gmail.com;

Contributing authors: laurent.cangemi@ifpen.fr;

francois.jouve@u-paris.fr ;

†These authors contributed equally to this work.

Abstract

Homogenization method is applied to topology optimization of a weakly coupled two physics problem, where structures are made of periodically perforated material. The microscopic periodic cell is macroscopically modulated, where the design is characterized by the material density and its homogenized Hooke's law at each point of the domain. The coupling is weak because the two physics involved are solved consecutively: first, the coupled fluid is determined using Biot-Darcy's law and second, the fluid-structure problem by solving the linear poro-elasticity system; our aim is to optimize the homogenized formulation of this two-physic problem. This approach permits a computationally low cost of evaluation of load sensitivities using the adjoint-state method. Numerical two-dimensional test cases are presented using the alternate directions algorithm. It is demonstrated how the implementation can address a variety of design problems.

Keywords: Topology optimization, multi-scale, periodic homogenization, porous medium, adjoint methods, fluid-structure interaction.

1 Introduction

The ambition to develop simulation methods making it possible to predict the integrity or properties of use (mechanical, diffusive, thermal, electromagnetic, vibratory, etc.) of structures (industrial or natural), materials or processes involved in the development of new advanced technologies is growing consistently. Herein, homogenization-based method is proposed to investigate shape optimization problems for a weakly coupled model of fluid flow and structure strain and, making it possible to consider a weak coupling between the two physics at stake because one can assume that the fluid domain is fixed at first order. However, we should bear in mind that this weak coupling is a major simplification and therefore reduces the computational cost.

A comprehensive overview of shape optimization with the homogenization method is provided by [1] and, for a general summary of the homogenization method, we refer the reader to [2–7] and references therein. Note that, this approach provides a consistent way for computing effective material with microstructures (composite materials) and that, once the optimal composite is obtained by homogenization-based topology optimization method, we might need to dehomogenize the solution: see [8], for periodically perforated materials. The design method described in this paper is strongly inspired by the works mentioned above as well as being related to modern production techniques such as additive manufacturing.

A typical shape optimization problem arising in this context involves an objective function, depending on the geometries of the fluid and solid subdomains and, where the whole domain is described by a density function (material density) that can take on values in the interval $[0, 1]$, which has to be minimized under some constraints (e.g., volume or mass constraints). This allows to compute the sensitivities with respect to design variables using the adjoint-state method [1, 9, 10], introducing adjoint states. For these adjoint states, which are to be solved, it turns out that the coupling is reversed for the adjoint system: the elasticity is solved first, followed by the fluid model.

Shape optimization that involve pressure-loaded boundaries has been conducted also by [11–23]. In [11, 16–18, 20], the authors deduce the topology or layout based on boundary motion and, using in [11, 16, 18], the iso-density method to identify the pressure loading facets: Bézier spline curves were used to describe the pressure-loaded facets. This allows in [11, 16], to evaluate the sensitivities with respect to design variables using the finite difference formulation and, in [18], to provide an analytical method to calculate load sensitivities. Note that in [11, 16, 18], the considered sensitivities were restricted to only the pressure-loaded boundaries.

In contrast, the works in [17, 19, 20] do not account for load sensitivities within their topology optimization setting: in [17], the pressure-loaded facets are predefined and, an additional set of variables is used, which are optimized along with the design variables; whereas in [20], an element-based search method is employed to identify the pressure-loaded facets and in [19], an algorithm

based on digital image processing and regional contour tracking is proposed to generate the pressure loading surface.

On the other hand, in [12], the authors deduce the topology optimization based on binary structures method to design structures that consider buckling constraints and loaded by design-dependent fluid pressure loads: it adopts binary design variables and handles multiple constraints solved by an integer linear programming scheme, where sensitivity filtering method is proposed.

In contrast to methods using boundary motion, in [13–15], the authors deduce the topology based on level-set methods: an implicit boundary description is available and, using to identify the pressure load. In [13], the Distance Regularized Level Set Evolution is proposed to capture the structural boundary and, using the zero level contour of a level-set function to represent the loaded-pressure boundary but did not account load sensitivities; whereas in [14], the Laplace’s equation approach is employed to compute hydrostatic fluid pressure fields and, also, a flood fill procedure to capture the solid/fluid interface: shape sensitivities in conjunction with ersatz material interpolation method are used within their approach. Recently in [15], Hadamard’s method of shape differentiation is applied to shape and topology optimization of a coupled thermal fluid-structure problem in a level set mesh evolution framework: sensitivity analysis is performed with respect to the geometry of the interface between the fluid and solid domain, using the Hadamard’s method of shape differentiation, introducing adjoint states.

Moreover, unlike boundary motion or level-set methods, in [21, 22], the authors deduce the topology using density-based approach: shape optimization problems are transformed to material distribution problems using fictitious composite materials and, without identifying loading surfaces directly. In [21], a density-based topology optimization is proposed to design both structures and compliant mechanisms loaded by design-dependent pressure loads: Darcy’s law in conjunction with a drainage term is proposed to treat the pressure loads, which are transferred into a design dependent pressure field using a partial differential equation, which is solved using the finite element method; the load sensitivities are computed using the adjoint-variable method. Recently in [22](2023), is developed per the approach first reported in [21], a MATLAB implementation TOPress, using the method of moving asymptotes.

In contrast, the density-based method presented in [23] is based on true composite materials: two material constituents, substance and void, are considered, and the microscopic optimal void distribution is considered. An important feature of the procedure is that the homogenization method is applied to determine macroscopic constitutive equations for the material with microscopic material constituents. In [23], the porous material is described as the Biot continuum derived by the homogenization of two decoupled problems: deformation of a porous solid saturated by a slightly compressible static fluid, first and, Stokes flow through the rigid porous structure, second. The effective medium (composite) properties are given by the drained skeleton elasticity, the Biot stress coupling, the Biot compressibility coefficients, and by the hydraulic

permeability of the Darcy flow model: these are computed using characteristic responses of the representative unit cell constituted by an elastic skeleton (solid) and by the fluid channel (void); the adjoint-state method is proposed to evaluate sensitivities of objective functions constituted by the Biot model coefficients with respect to the underlying pore shape described by a B-spline box which embeds the whole representative cell and, where the gradient-based method is employed to solve the optimization problems: the shape derivatives of the homogenized coefficients are derived using the shape sensitivity technique and the material derivative approach.

In this article, we present a new approach to design structures loaded by design-dependent pressure loads and, this falls within the general framework of density methods where phenomenological laws of equivalent media is derived by the homogenization method. In this regard, the presented approach falls within the framework of recent work in [21, 23] where Darcy’s flow model is used to describe the fluid flow. However, the approach in [21] is different since the continuous problem does not contain a model that explicitly couples the fluid pressure to the solid skeleton and thus, it induces difficulties in the modeling where a volumetric force is added intuitively in the elastic problem without it being explicitly defined as the result of a continuous physical law. Moreover, compared to [23], the porous material is described as the Biot-Darcy continuum derived by the homogenization of a weakly coupled two physics problem: deformation of a porous solid saturated by incompressible fluid pressure (satisfying Biot-Darcy’s law), first and, Biot-Darcy’s flow through the rigid porous structure, second. The effective medium properties are given by the undrained skeleton elasticity, the Biot stress coupling, the Biot coefficient, and by the hydraulic permeability of the Darcy flow model: these are computed using characteristic responses of the representative unit cell, namely a perforated hexagonal cell constituted by a solid phase and void; see Fig. 1. Hence, the fluid pressure can be seen as a pore pressure acting on the solid part of the ”equivalent porous material” through a Biot coefficient, which is density-dependent and, where the physical laws derived from the mechanics of porous media make it possible to link this coefficient to the local (matrix) and global (porous medium) moduli of compressibility of the solid system. This allows to provide sensitivities of general ”smooth enough” objection functions with respect to design variables using the adjoint-state method, introducing adjoint-states; the homogenized coefficients are derived using the Lagrangian method and the projected gradient algorithm: in [23], the shape sensitivity technique and the material derivative approach are employed. Of course, these shape derivatives are at the basis of our gradient-based alternate directions algorithm [1], which is used for our numerical simulations. In summary, we present the following aspects:

- homogenized Biot-Darcy’s law is used to characterize the fluid flow through a true composite material,
- we weakly couple the fluid loads to the linearized poro-elasticity system for the solid displacement,

- the approach facilitates computationally inexpensive evaluation of the load sensitivities with respect to design variables using the adjoint-state method, introducing adjoint-states,
- the flow coefficient, Biot's coefficient are derived by the homogenization method,
- the approach avoids explicit description of the pressure loading boundary,
- the robustness and efficiency of the approach is demonstrated through numerous design problems, using the alternate directions algorithm.

The remainder of this paper is structured as follows: in Section 2, we briefly recall the necessary ingredients of the homogenization approach and we explain our strategy. First, choose a parametrized periodicity cell. Second, we compute its effective properties for the entire range of its parameters. In Section 3, we give a precise account of the weakly coupled two physics model of fluid flow and structure deformation. In Section 4, first, we introduce the optimization problem formulation, which turns out to be a simple parametric optimization problem since our periodicity cell is parametrized. Second, we determined the associated sensitivity analysis. Section 5, is concerned with our topology optimization algorithm: an alternate direction algorithm, which successively computes the stress field through the solving of a weakly coupled two-physic problem. Finally, our numerical results are presented in Section 6: 2-d computations are displayed of various design problems involving fluid-pressure loaded structures and small deformation; and we summarize our findings and give an outlook in Section 7.

2 Periodic homogenization

The mathematical framework of the homogenization theory can be found in [1]; here, we briefly present the principles of this approach and explain our strategy. We restrict our analysis to the 2-d case and to locally periodic-hexagonal composites. Note that, it should be possible to adapt the whole method (or at least part of it) to periodic-square cells or to 3-d case. Our aim is to determine the homogenized physical properties of such materials when varying their parameter; a preprocessing stage, which can be performed off-line. This is independent of the objective function, computational domain, applied loads or boundary conditions. The Hooke's laws are computed by solving the so-called cell problems, that describe the deformation at the scale of the microstructure, which is a very classical task in homogenization theory.

2.1 Set of admissible microstructures

From now on, we restrain our analysis to a simple class of composites already introduced in [26]: an hexagonal cell perforated by a smooth hexagonal central hole, known as the smooth honeycomb cell, repeated periodically on the whole space.

Let Y be the periodic smooth honeycomb cell: similar to the classical honeycomb cell (an hexagonal cell with perforated hexagonal central hole), except that the interior corners of the perforated hexagonal hole are rounded (see Fig. 1 and Fig. 2). As a consequence, if the density $\theta \in [0, 1]$, tends to 1, the central smooth hexagon tends to a circle with a diameter going to 0. However, because of its rounded corners, the smooth honeycomb can not reach complete void: θ going to zero is excluded. In this context, for practical reason, the smooth honeycomb is (contrary to the classical one, which is parametrized by the density) parametrized by another parameter $h \in [0, 1]$, homogeneous to a distance. Indeed, in order to design this kind of cell, a parametric curve Γ_h which depends on h is introduced and represents the boundary of the perforated smooth central hole.

We now introduce some notations before giving its polar equation. Let $v(t) = (\cos(t), \sin(t))^T$ and n_i (for $i \in \{0, 1, 2\}$) represent the normal vectors of the three diagonals of $Y(h)$, that are:

$$n_0 = \begin{pmatrix} 0 \\ 1 \end{pmatrix}, \quad n_1 = \begin{pmatrix} \frac{\sqrt{3}}{2} \\ \frac{1}{2} \end{pmatrix}, \quad n_2 = \begin{pmatrix} \frac{\sqrt{3}}{2} \\ -\frac{1}{2} \end{pmatrix}. \quad (1)$$

The polar equation of the parametric curve Γ_h (of smooth hexagon hole) is defined by:

$$r(t) = h \frac{\sqrt{3}}{2} \left(\sum_{i=0}^2 |v(t) \cdot n_i|^{k(h)} \right)^{-\frac{1}{k(h)}} \quad \text{with } t \in [0, 2\pi], \quad (2)$$

where k is a positive coefficient, which depends on h : for this work, we took $k(h) = 4 + 20h^2$. Note that h is homogeneous to a distance, similar to the parameter

$$m = \frac{\sqrt{3}}{2} (1 - \sqrt{1 - \theta}),$$

which denotes the relative width of bars with respect to the size of the periodic cell $Y(h)$; see Fig. 1(b).

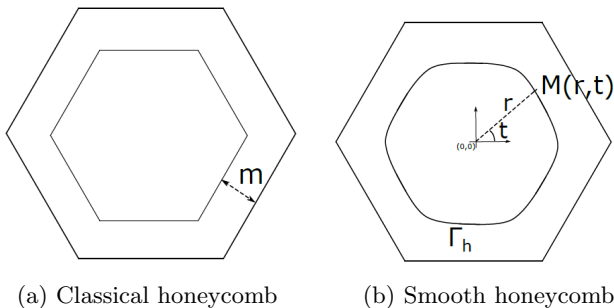


Fig. 1 Isotropic design cells (images taken from [26])

In the following, we give some remarks over the polar equation of the parametric curve Γ_h , which can be extended to other polygons. Let \mathcal{H} be a regular unit hexagon, namely, the set of all points such that the maximal distance of a point in \mathcal{H} from the three diagonals is equal to $\frac{\sqrt{3}}{2}$. Let $M(r, t)$ be a point, with its polar coordinate denoted by (r, t) . Thus, M is a point in \mathcal{H} if and only if, its polar coordinate (r, t) satisfies

$$r \max_i |v(t) \cdot n_i| = \frac{\sqrt{3}}{2}. \quad (3)$$

Hence, the polar equation of \mathcal{H} verifies

$$r(t) = \frac{\sqrt{3}}{2} (\max_i |v(t) \cdot n_i|)^{-1}. \quad (4)$$

As a consequence, we get that

$$\left(\sum_{i=0}^2 |v(t) \cdot n_i|^k \right)^{-\frac{1}{k}} \rightarrow_{k \rightarrow \infty} \max_i |v(t) \cdot n_i|. \quad (5)$$

Note that, the polar equation of Γ_h comes from combining the polar equation of \mathcal{H} and the above limit; the parameter h is added in order to adjust the diameter of its inner hole. Here, our interest for the smooth honeycomb relies on its smooth rounded corners, known to generate lower local concentration stress [27, 28] compared to the classical honeycomb.

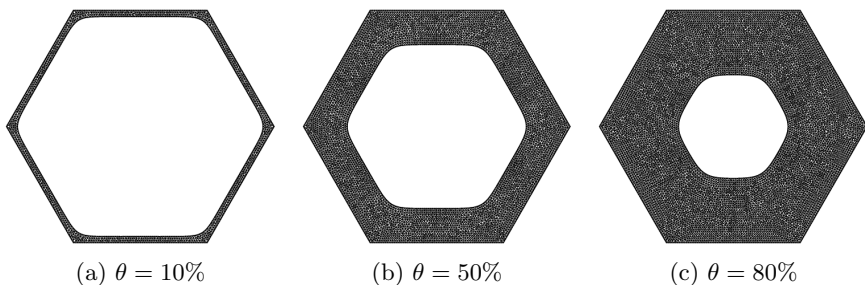


Fig. 2 The Smooth honeycomb cell for different values of the density θ

2.2 Cell problem and homogenized elasticity tensor

Here, we only give a few important results on the theory of homogenization; the interested reader will find more details in [1].

Assume that, in a given macroscopic domain $\Omega \subset \mathbb{R}^N$ ($N = 2$), there is a periodic distribution of holes inside an isotropic elastic material, with constant elastic tensor A . Let $\epsilon > 0$ be the periodic size and let Y be the periodic

pattern: a regular smooth hexagon. The periodicity of Y , is defined by the same displacement on two opposite and parallel faces; hence, for the hexagonal cell, there are three directions of periodicity; see Fig. 1. Let Y_0 be the solid part in Y and, we denote by $|Y|$, the volume of the periodic cell Y ; and, let Γ be the boundary of the holes (i.e., the interface solid/void) and \mathbf{n} be the normal vector to the boundary Γ .

In addition, assume that whenever ϵ tends to zero, the porous medium can be considered homogeneous, with effective tensor denoted $A^*(x)$. To compute the homogenized tensor A^* , one needs the so-called correctors w_{ij} , corresponding to the local displacements in the periodic cell Y , defined for each pair $(i, j) \in \{1, \dots, N\}$ as the solutions to the following set of equations:

$$\begin{cases} \operatorname{div}(A(e_{ij} + e(w_{ij}))) = 0 & \text{in } Y_0 \\ A(e_{ij} + e(w_{ij})) \cdot \mathbf{n} = 0 & \text{on } \Gamma \\ y \mapsto w_{ij}(y) & Y_0\text{-periodic,} \end{cases} \quad (6)$$

where $e_{ij} = \frac{1}{2}(e_i \otimes e_j + e_j \otimes e_i)$ represents the basis of the symmetric tensors of order 2. As a consequence, the variational formulation associated to (6) is defined as follows: find $w_{ij} \in H_{\#}^1(Y, \mathbb{R}^N) = \{w \in H^1(Y, \mathbb{R}^N) \mid w \text{ is } Y\text{-periodic}\}$ such that

$$\forall \phi \in H_{\#}^1(Y, \mathbb{R}^N) \quad \int_Y A e(w_{ij}) : e(\phi) + \int_Y A e_{ij} : e(\phi) = 0, \quad (7)$$

which admits a unique solution (up to a rigid displacement field). The entries of $A^*(x)$ are then defined in terms of the correctors w_{ij} , solutions of (6), that are:

$$A_{ijkl}^* = \frac{1}{|Y|} \int_Y A(e_{ij} + e(w_{ij})) : (e_{kl} + e(w_{kl})) \, dy \quad \forall i, j, k, l \in \{1, \dots, N\} \quad (8)$$

We emphasize that, to compute the homogenized tensor A^* , only three of its coefficients are needed (e.g., A_{1111}^* , A_{1122}^* and A_{1212}^*) to fully characterize A^* . However, all the coefficients were computed to demonstrate that the homogenized material is isotropic (or quasi-isotropic). Herein, we use a linear material model with Young's modulus $\mathbf{E} = 12 \times 10^9 \text{Nm}^{-2}$ (i.e., 12GPa) and Poisson's ratio $\nu = 0.35$. We recall that, if the effective tensor A^* is isotropic, it can be written as:

$$A^* = 2\mu^* I_{2N} + \left(\kappa^* - \frac{2\mu^*}{N}\right) I_N \otimes I_N, \quad (9)$$

where κ^* and μ^* are the bulk and shear moduli of the homogenized Hooke's law A^* , with its first Lamé coefficient defined by: $\lambda^* = \kappa^* - \frac{2\mu^*}{N}$. I_{2N} and I_N in Eq. (9), represent the fourth order symmetric identity and the identity tensor

of order N . The entries are defined by:

$$\begin{cases} \mu^* = A_{ijij}^* \\ \lambda^* = A_{iijj}^* \\ \kappa^* = A_{iijj}^* + \frac{2}{N} A_{ijij}^* \end{cases} \quad \forall i, j \in \{1, \dots, N\} \quad (10)$$

where the isotropy of A^* , is satisfied if we have the following relations:

$$\forall i, j, k, l \in \{1, \dots, N\} \quad \begin{cases} A_{ijkl}^* = A_{klij}^* \\ A_{iijk}^* = 0 \\ A_{iiii}^* = A_{jjjj}^* \\ A_{iijj}^* = A_{kkll}^*; \quad \forall i \neq j, k \neq l \\ A_{iiii}^* = A_{ijij}^* + A_{iijj}^* \end{cases} \quad (11)$$

Numerical results

The homogenized tensor $A^*(\theta)$ has been computed for the periodic cell Y , for discrete values $(\theta_i)_{i=1, \dots, n}$ of θ : a preprocessing stage, which is performed offline. Herein, a table of size $n = 1000$ is built, which is then used to compute the local composites during the optimization process: a linear interpolation approach is used to update the homogenized tensor. The errors with respect to the equalities in (11) are depicted on Fig. 3.

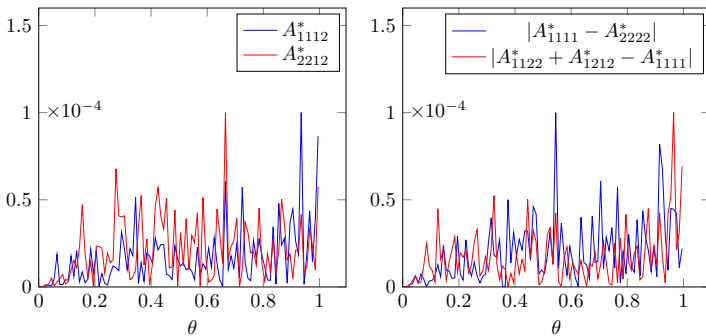


Fig. 3 The errors with respect to the equalities in (11), for different values of the density θ

2.3 Cell problem and homogenized model in conductivity

We now consider a model problem of pressure conductivity, similar to the elasticity system defined in Eq. (2.2). Starting from a microscopic description of a problem, one seeks a macroscopic or effective model problem in conductivity K^* which can be the permeability of a fluid flowing through a porous material composed of solid and fluid one. We introduce the so-called cell problems, similar to the elasticity system. Howbeit, since the considered cell Y is isotropic,

only one of its coefficient (e.g., $(K^*)_{11}$) could be computed in order to fully characterize K^* .

Let $(e_i)_{i=1,\dots,N}$ be the canonical basis of \mathbb{R}^N and, for each unit vector e_i , we consider the following conductivity problem in the periodic cell Y :

$$\begin{cases} -\operatorname{div}(K(e_i + \nabla w_i)) = 0 & \text{in } Y \\ y \mapsto w_i(y) & Y \text{ periodic,} \end{cases} \quad (12)$$

where $w_i(y)$ is the local variation of pressure created by an averaged (or macroscopic) gradient e_i . The homogenized conductivity K^* is then given in terms of the correctors w_i , solutions of (12), defined by:

$$(K^*)_{ij} = \frac{1}{|Y|} \int_Y K(e_i + \nabla w_i) : (e_j + \nabla w_j) \, dy \quad \forall i, j \in \{1, 2\} \quad (13)$$

where the tensor K^* describes the effective or homogenized properties of the heterogeneous microstructure of periodic size ϵ . We recall that, K^* does not depend on the choice of domain Ω , source term f_f , or boundary conditions and, $Y = Y_0 \cup (Y \setminus Y_0)$ is a disjoint reunion of the solid and void, where K can be defined as follows:

$$K(y) = \begin{cases} \epsilon_0 & \text{in } y \in Y_0 \\ 1 & \text{in } y \in Y \setminus Y_0 \end{cases} \quad (14)$$

where ϵ_0 is a given threshold.

Numerical results

The tensor K^* has been computed over the smooth honeycomb for discrete values of θ . For this latter, note that K^* is a matrix of order N , proportional to the identity matrix:

$$K^* = \alpha^* I_N, \quad \text{where } \alpha^* = (K^*)_{11} = (K^*)_{22},$$

because the chosen local cell is isotropic and, K^* can be identified to the scalar α^* . On Fig. 4, we plot the homogenized flow $\frac{\alpha^*}{\|\alpha^*\|_\infty}$ (which is normalized) in comparison to the defined flow coefficient $K_D^*(\theta) = \min\left(\frac{\epsilon_0 + (1 - \epsilon_0)(1 - \theta)}{\theta}, K_\infty\right)$ for discrete values $(\theta_i)_{i=1,\dots,n}$, with $\|\alpha^*\|_\infty = \sup_{\theta_i} \alpha^*(\theta_i)$. See Section 3.1, for more details. As expected, $\frac{\alpha^*}{\|\alpha^*\|_\infty}$ is a decreasing function with respect to the density θ . We emphasize that, the residuals $|(K^*)_{11} - (K^*)_{22}| \leq 10^{-6}$ and $(K^*)_{12} \leq 10^{-3}$ are sufficiently small, which validates the isotropy assumption. We note that, the homogenized flow coefficient $\frac{\alpha^*}{\|\alpha^*\|_\infty}$ can be approximated by the determined flow coefficient K_D^* .

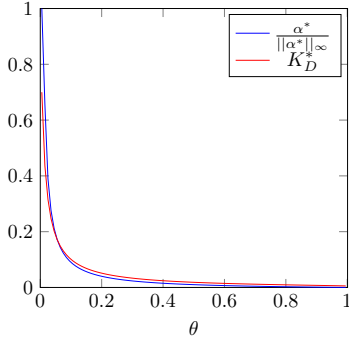


Fig. 4 The homogenized flow $\frac{\alpha^*}{\|\alpha^*\|_\infty}$ in comparison to the determined flow K_D^* , for different values of the density θ

3 Setting of the two-physic problem

Here, we investigate the weakly coupled model of fluid flow and structure strain. First, the fluid flow is described using the Biot-Darcy's law, then, the linearized poro-elasticity system (for the mechanical displacement) is characterized.

Let Ω be a fixed domain in \mathbb{R}^N ($N = 2$ or 3), filled with composite material periodically perforated by the hexagonal cell and, characterized by one parameter θ : the material density, which has to be optimized. Let \mathbf{n} be the normal vector to the boundary $\partial\Omega$, pointing outward to the domain Ω . The domain Ω is described by two physical variables which are governed by two coupled models, that are:

- the motion of the fluid inside the domain, described by the pressure field p , satisfying the Biot-Darcy's law
- the deformation of the solid phase, as a result of the stress exerted by the fluid part, characterized by a mechanical displacement u

The physical equations chosen for the modeling of the state variables p and u with their relevant set of boundary conditions are now described in strong form in Section 3.1 and Section 3.2.

3.1 Hydraulic law of Biot-Darcy-type for the pressure variable

We give a precise account of the weakly coupled fluid model that is based on the Biot-Darcy's law; the effect of which is to establish the pressure field as a function of material density θ .

From a fluid point of view, Darcy's law describes the fluid ability to flow through a porous media such as soil, sandstone or rock; it states that the fluid flowing through a unit area is directly proportional to the pressure drop per unit length ∇p and, inversely, that the resistance of the porous medium is

proportional to the flow μ ([31]), which is defined by:

$$\mathbf{q} := -\frac{\kappa_f}{\mu_f} \nabla p = -K_D^* \nabla p, \quad (15)$$

where \mathbf{q} , κ_f , μ_f , ∇p , and K_D^* characterize the flux (ms^{-1}), permeability (m^2), fluid viscosity ($Nm^{-2}s$), pressure gradient (Nm^{-3}), and the flow coefficient ($m^4N^{-1}s^{-1}$) (which defines the fluid ability to flow through a porous medium). In order to smoothly and continuously distribute the pressure drop in fluid domain and differentiate between solid and void phase in the whole domain, the homogenized flow coefficient $K^*(\theta(x))$ (which we numerically compute, see Section 2.3) is approximated by a smooth function, that is:

$$K_D^*(\theta(x)) := \min \left(\frac{\epsilon_0 + (1 - \epsilon_0)(1 - \theta(x))}{\theta(x)}, K_\infty \right), \quad (16)$$

where ϵ_0 and K_∞ are given thresholds; here, $\epsilon_0 = 10^{-4}$ and $K_\infty = 10^3$. We recall that, an homogenization method was performed on the flow coefficient and, we notice that the homogenized flow coefficient K^* can be characterized by the above function; see Fig. 4. We now assume that the density-dependent pressure field p , satisfies a Biot's law, that is:

$$p := Mm - Mbe_{vol}, \quad (17)$$

where M , m and e_{vol} are smooth enough functions related to the material density θ defined by:

$$m(\theta) := (1 - \theta)\rho, \quad M(\theta) := \frac{1 - \theta}{\kappa_v} - \frac{b(\theta) - (1 - \theta)}{\kappa_s}, \quad e_{vol} := \nabla \cdot \mathbf{u}, \quad (18)$$

where ρ , κ_v , κ_s and $e_{vol} = \text{div}(\mathbf{u})$, represent the density of the flux, compressibility of the void and solid phase and, the volume variation of the solid phase at each finite element; the parameters M and b are the so called Biot modulus and Biot coefficient. The Biot's law (17) is assumed to be related to Darcy's law (15), defined as follows:

$$\mathbf{q} := mv_f = -K_D^* \nabla p, \quad (19)$$

where v_f represents the velocity of the flux. Thus, the above equation (19), allows to render gradually the pressure drop from the inner pressure boundary to the outer pressure boundary. Note that this penetrating pressure of Biot-Darcy's law is similar to that introduced in [21], which makes this pressure loading boundary a smeared-out version of an applied pressure load on a sharp boundary. In addition to the Biot-Darcy equation (19), we assume that the state equation satisfies the law of conservation of mass in view of

incompressible fluid, that is:

$$\frac{\partial m}{\partial t} := -\operatorname{div}(\mathbf{q}) = \operatorname{div}(K_D^* \nabla p) \quad (20)$$

Consequently, we derive from the Biot's law (19), the equation:

$$\frac{\partial p}{\partial t} := M(\theta(x)) \frac{\partial m}{\partial t} - M(\theta(x)) b(\theta(x)) \frac{\partial e_{vol}}{\partial t}, \quad (21)$$

and for sake of simplicity, we assume that our fluid model is stationary and satisfies the law of conservation of mass (in view of incompressible fluid), that is:

$$\frac{\partial m}{\partial t} := -\operatorname{div}(\mathbf{q}) = \operatorname{div}(K_D^* \nabla p) = 0 \quad (22)$$

We now assume that our design domain is filled with isotropic composite material and, as such the Biot's coefficient $b(\theta)$ can be defined as follows:

$$b(\theta(x)) := 1 - \frac{\kappa_s(\theta(x))}{\kappa}, \quad (23)$$

where κ and $\kappa_s(\theta(x))$ represent the bulk moduli of the solid phase A and the homogenized tensor $A^*(x)$. Note that, $A^*(x)$ tends to A when $\theta(x)$ tends to 1; thus, $\kappa_s(\theta)$ tends to κ ; this article should be approached within such background, that is, we assume that the weakly coupled fluid model is defined in the particular case of a porous isotropic medium. It is worth to note that the Biot modulus (18) and coefficient (23) are explicitly defined only in the case of a linear isotropic elastic matrix microscopically homogeneous which is the case herein. By using the Biot-Darcy's law (22), the weakly coupled fluid model can be defined by:

$$\text{(Biot-Darcy)} \begin{cases} -\operatorname{div}(K_D^* \nabla p) = 0 & \text{in } \Omega, \\ p = p_0 & \text{on } \Gamma_D^f, \\ \mathbf{q}_\Gamma \cdot \mathbf{n} = f_f & \text{on } \Gamma_N^f, \\ \mathbf{q}_\Gamma \cdot \mathbf{n} = 0 & \text{on } \Gamma^f = \partial\Omega \setminus (\Gamma_D^f \cup \Gamma_N^f), \end{cases} \quad (24)$$

In (24), f_f is an applied Neumann isoflux condition for the pressure variable p . The boundary of the fluid phase is the disjoint reunion

$$\partial\Omega = \Gamma_D^f \cup \Gamma_N^f \cup \Gamma^f$$

of a Dirichlet (or inlet) part Γ_D^f where the flow enters with a given pressure $p = p_0$, a Neumann (or outlet) part Γ_N^f where normal stress is imposed and, free interface Γ^f of $\partial\Omega$. At this stage it is assumed that the deformation of the solid domain is sufficiently small so that no slip boundary conditions hold on:

$\mathbf{q}_\Gamma \cdot \mathbf{n} = 0$. Therefore, the variable p depends solely on the material density $\theta(x)$, for all $x \in \Omega$.

3.2 Elasticity with fluid-structure interaction

Finally, the pressure variable p determines the displacement u of the solid part in Ω , which we assume to be isotropic poro-elastic composite material, with homogenized Lamé coefficients denoted λ^* , μ^* . As a consequence, the weakly coupled fluid-elastic model is defined by the linear poro-elasticity (of Biot-Coussy type):

$$\begin{cases} -\operatorname{div}(\sigma(u)) = -b\nabla p & \text{in } \Omega, \\ u = u_0 & \text{on } \Gamma_D^s, \\ \sigma(u) \cdot \mathbf{n} = f_s & \text{on } \Gamma_N^s, \\ \sigma(u) \cdot \mathbf{n} = 0 & \text{on } \Gamma^s, \end{cases} \quad (25)$$

where the homogenized stress and strain tensors are given by:

$$\sigma(u) = A^* : e(u) = 2\mu^* e(u) + \lambda^* \operatorname{Tr}(e(u))I, \quad (26)$$

$$e(u) = \frac{1}{2}(\nabla u + \nabla^t u) \quad (27)$$

where I is the identity matrix. Note that, the source term in (25) is the stress exerted by the fluid part; the boundary $\partial\Omega$ is split into a Dirichlet part Γ_D^s where a displacement $u = u_0$ is prescribed, a Neumann part Γ_N^s where a stress f_s is imposed and, a free part Γ^s .

Remark 1 The above model is a simplified version of a genuine fluid-solid coupling between the solid and fluid phase. A more accurate description of fluid-structure interaction would feature a transition regime and inertia regime:

$$\mathbf{q} := m v_f + \rho C_{for} v_f^2$$

where C_{for} is an inertia parameter of the fluid flow, called Forchheimer coefficient. For sake of simplicity, we opted for a simplified version, which is justifiable insofar as we wish to obtain a first qualitative result of microstructure without however, sizing as accurately as possible the system. Hence, the Forchheimer coefficient C_{for} is neglected.

4 The optimization problem formulation and its sensitivity analysis

We present the optimization problem formulation associated to the weakly coupled fluid-structure problem and discuss the sensitivity analysis for such design problems. The announced goal is the resolution of relaxed unconstrained

version of the original optimization problem, that is:

$$\begin{aligned} & \min_{\theta} J^*(\theta, p(\theta), u(\theta)) \\ \text{s.t. } & \begin{cases} g_i(\theta, p(\theta), u(\theta)) = 0, & 1 \leq i \leq p, \\ h_j(\theta, p(\theta), u(\theta)) \leq 0, & 1 \leq j \leq q, \end{cases} \end{aligned} \quad (28)$$

where J^* , g_i and h_j are arbitrary relaxed shape objective and constraint functionals. For its resolution, we shall rely on the alternate minimization algorithm [1] detailed in Section 5.1, which (like any other first order optimization method) requires the knowledge of the shape derivatives of the above functionals: here, the adjoint-state method is used to determine the sensitivities of the objective functions and constraints with respect to the design variable θ . It is worth to mention that, likewise, in [23], the authors employed the adjoint-state method to evaluate the sensitivities of objective functions (constituted by the Biot model coefficients with respect to the underlying pore shape described by a B-spline box which embeds the whole representative cell) and the gradient-based method to solve the optimization problems; howbeit, the considered shape derivatives of the homogenized coefficients are different: they rely on the shape sensitivity technique and the material derivative approach. Herein, the "shape" is describe by the density θ and, the shape derivatives are performed using the Lagrangian method and the projected gradient algorithm. In this context of the adjoint-state method, this means computing the derivative of the mapping:

$$\theta \mapsto J^*(\theta, p(\theta), u(\theta)),$$

where θ belongs in general to set of admissible design variables \mathcal{U}_{ad} , that is:

$$\mathcal{U}_{ad} := \left\{ \theta \in L^\infty(\Omega; \mathbb{R}_+^*) \mid \theta(x) \in [0, 1], \forall x \in \Omega \right\}$$

In contrast, note that in [23], a general optimization variable α is introduced which is related to the effective medium parameters: it determines the homogenized coefficients for any position $x \in \Omega$.

4.1 A fully Lagrangian setting for computing shape derivatives

Although very common and widely used in the literature, an issue with the adjoint-state method [1, 9] is that the computation of the shape derivatives depend very much on the assumptions made on the nature of the considered objective functional J^* ; different type of functionals may lead to different strong forms for the adjoint equations where this fact is exemplified, which imposes to redo the analytical derivation whenever the objective function is modified, and to update the numerical implementation accordingly. Here, we use a fully Lagrangian setting to compute rigorously the shape derivative of very general objective functionals in the simplified setting of Section (3.1) and

Section (3.2). The shape sensitivities of the state variables $p(\theta)$ and $u(\theta)$ are calculated first, in order to obtain the shape derivative of an arbitrary objective functional in volume form. Then, under sufficient regularity assumptions, the well-known adjoint-state method together with suitable augmented Lagrangian functional yield general shape derivative formulas.

4.2 A modified objective functional and Lagrangian derivative

In a gradient-based topology optimization, it is essential to determine sensitivities of the objective functional and the constraints with respect to the design variable(s). The starting remark is that the relaxed functional J^* , although appearing naturally in the formulation of the optimization problem (28) is not so convenient for the mathematical analysis. Indeed, the domain of definition of $J^*(\theta, \dots)$ is a functional space which depends on the first argument θ . In order to discuss the precise mathematical settings of our multiphysic system, we introduce the functional spaces which are required for the fluid-structure, that are:

$$\begin{aligned} V(\Gamma_D^f) &= \{q \in H^1(\Omega) \mid q = 0 \text{ on } \Gamma_D^f\}, \text{ for the pressure variable } p \\ V(\Gamma_D^s) &= \{v \in H^1(\Omega)^N \mid v = 0 \text{ on } \Gamma_D^s\}, \text{ for the displacement } u \end{aligned} \quad (29)$$

and, we consider the subspace

$$H^{1/2}(\Gamma_N^s) = \{v|_{\Gamma_N^s} \mid v \in V(\Gamma_D^s)\}$$

and its dual space $H^{-1/2}(\Gamma_N^s)$; as well the affine spaces associated to the non-homogeneous Dirichlet boundary data $u_0 \in H^{1/2}(\Gamma_D^s; \mathbb{R}^N)$ and $p_0 \in H^{1/2}(\Gamma_D^f; \mathbb{R})$ featured in (3.1)-(3.2). The state variables p and u are then solutions to the following variational problems: find $(p, u) \in \{p_0 + V(\Gamma_D^f), u_0 + V(\Gamma_D^s)\}$, such that

$$\begin{cases} \int_{\Omega} K_D^* \nabla p \cdot \nabla q + \int_{\Gamma_N^f} f_f q \, dx = 0, & \forall q \in V(\Gamma_D^f), \\ \int_{\Omega} \sigma(u) \cdot e(v) \, dx - \int_{\Gamma_N^s} f_s \cdot v \, ds + \int_{\Omega} b \nabla p \cdot v \, dx = 0, & \forall v \in V(\Gamma_D^s) \end{cases} \quad (30)$$

In order to address the sensitivity of an arbitrary objective function, the classical idea is to work within a Lagrangian framework. Therefore, we consider the corresponding Lagrangian, which is an augmented function of the objective function, that is:

$$\begin{aligned} \mathcal{L}(\hat{\theta}, \hat{u}, \hat{u}, \hat{p}, \hat{p}, \ell) &= J^*(\hat{\theta}) + \int_{\Omega} \hat{u} (-div(\sigma(\hat{u}) + b(\hat{\theta}) \nabla \hat{p})) \, dx \\ &+ \int_{\Omega} \hat{p} (-div(K_D^*(\hat{\theta}) \nabla \hat{p})) \, dx + \ell \left(\int_{\Omega} \hat{\theta} \, dx - \Theta \right), \end{aligned} \quad (31)$$

where $(\hat{\theta}, \hat{u}, \hat{p}, \hat{p}) \in L^\infty(\Omega; \mathbb{R}) \times H_0^1(\Omega; \mathbb{R}^N)^2 \times H_0^1(\Omega; \mathbb{R})^2$ are independent variables and, the positive scalar ℓ is the Lagrange multiplier designed to satisfy the volume constraint. Note that, the objective function $J^*(\hat{\theta})$ depends upon the state variables u and p . By integration by parts, we get

$$\begin{aligned} \mathcal{L}(\hat{\theta}, \hat{u}, \hat{p}, \hat{p}, \ell) &= J^*(\hat{\theta}) + \int_{\Omega} (\sigma(\hat{u}) : e(\hat{u}) + b(\hat{\theta})\nabla\hat{p} \cdot \hat{u}) dx \\ &\quad + \int_{\Omega} K_D^* \nabla\hat{p} \cdot \nabla\hat{p} dx + \ell \left(\int_{\Omega} \hat{\theta} dx - \Theta \right), \end{aligned} \quad (32)$$

where the homogenized objective function J^* is assumed to be smooth enough function, otherwise we cannot apply the adjoint-state method.

4.3 Sensitivity analysis for the two-physic problem

The sensitivities are evaluated by differentiating the Lagrangian (32) with respect to state variables u and p in directions $\phi_u \in H^1(\Omega)^N$ and $\phi_p \in H^1(\Omega)$. Let $(u, \underline{u}) \in H_0^1(\Omega; \mathbb{R}^N)^2$ be a stationary point of \mathcal{L} . Then, the derivative of the Lagrangian (32) with respect to u , in direction $\phi_u \in H^1(\Omega)^N$ is given by:

$$\left\langle \frac{\mathcal{L}}{\partial u}, \phi_u \right\rangle = \left\langle \frac{\partial J^*}{\partial u}, \phi_u \right\rangle + \int_{\Omega} \left\langle \frac{\partial \sigma(\hat{u})}{\partial u}, \phi_u \right\rangle : e(\hat{u}) dx, \quad (33)$$

while the derivative with respect to p , in direction $\phi_p \in H^1(\Omega)$ is given by:

$$\left\langle \frac{\mathcal{L}}{\partial p}, \phi_p \right\rangle = \left\langle \frac{\partial J^*}{\partial p}, \phi_p \right\rangle + \int_{\Omega} b \nabla \phi_p \cdot \hat{u} dx + \int_{\Omega} K_D^* \nabla \phi_p \cdot \nabla \hat{p} dx, \quad (34)$$

which when equations (33) and (34) vanish, are nothing more than the variational formulation associated to the adjoint-states. Moreover, the derivatives with respect \underline{u} and \underline{p} , in directions $\phi_u \in H^1(\Omega)^2$ and $\phi_p \in H^1(\Omega)$ are simply the state equations, that are:

$$\left\langle \frac{\partial \mathcal{L}}{\partial \underline{u}}, \phi_u \right\rangle = \int_{\Omega} (\sigma(\hat{u}) : e(\phi_u) + b(\hat{\theta})\nabla\hat{p} \cdot \phi_u) dx, \quad (35)$$

and

$$\left\langle \frac{\partial \mathcal{L}}{\partial \underline{p}}, \phi_p \right\rangle = \int_{\Omega} K_D^* \nabla\hat{p} \cdot \nabla\phi_p dx, \quad (36)$$

which when equations (35) and (36) vanish, is nothing more than the variational formulation associated to the state equations (24)-(25): note that to obtain the adjoint-state equations in [23], the optimality condition for the state variables is considered and, together with the state variables yield the adjoint state variables. Finally, the partial derivative of the Lagrangian \mathcal{L} with respect

to θ , in direction $\bar{\theta} \in L^\infty(\Omega; \mathbb{R})$ at the stationary point $(u, \underline{u}, p, \underline{p})$ is given by:

$$\left\langle \frac{d\mathcal{L}}{d\theta}, \bar{\theta} \right\rangle = \left\langle \frac{\partial J^*}{\partial \theta}, \bar{\theta} \right\rangle + \int_{\Omega} \left(\frac{\partial \sigma(\hat{u})}{\partial \theta} : e(\hat{u}) + \frac{\partial b}{\partial \theta} \nabla \hat{p} \cdot \hat{u} + \frac{\partial K_D^*}{\partial \theta} \nabla \hat{p} \cdot \nabla \underline{\hat{p}} dx + \ell \right) \bar{\theta} dx \quad (37)$$

Note that, Eq. (37) is defined using the adjoint-state method. As a consequence, the descent direction $\bar{\theta} = d\theta$ is defined by solving Eq. (37). The term $\left\langle \frac{\partial J^*}{\partial \theta}, \bar{\theta} \right\rangle$ is the partial derivative of the objective function J^* with respect to the density θ , in direction $\bar{\theta}$, while the term

$$\int_{\Omega} \left(\frac{\partial \sigma(\hat{u})}{\partial \theta} : e(\hat{u}) + \frac{\partial b}{\partial \theta} \nabla \hat{p} \cdot \hat{u} + \frac{\partial K_D^*}{\partial \theta} \nabla \hat{p} \cdot \nabla \underline{\hat{p}} dx + \ell \right) \bar{\theta} dx$$

is the adjoint. \hat{u} and \hat{p} are the adjoint-state variables, solutions to the adjoint equations (33)-(34) (which we have to solve first). We recall that ℓ is the Lagrange multiplier designed to satisfy the volume constraint at each iteration and, such a constraint is routinely handled in elementary calculus of variations: here, the dichotomy approach is employed.

5 Topology optimization of modulated periodic composite materials

Here, our numerical algorithm is proposed. We describe how the methodology applies to the weakly coupled two physics system of (24)-(25).

5.1 Alternate minimization method

The optimization problem (28) is solved using the alternate minimization algorithm [1].

5.1.1 Minimizing over the stress field

For given design field θ , the minimization with respect to the stress field σ amounts to solve the poro-linear elasticity problem (25), with a material of elasticity tensor equal to $A^*(x)$ in Ω and where, the design (θ, A^*) is computed by linear interpolation over a surrogate model of $A^*(\theta)$: a preprocessing stage, which is performed offline; see Section 2.2.

5.1.2 Minimizing over the density field

The minimization over the density field θ , for a given stress tensor σ , is performed using the projected gradient algorithm and, as the minimization problem (28) is not self-adjoint, one needs to define the associated adjoint

problem, which is defined using the adjoint-state method; see, Section 4. As a consequence, the descend direction $h = d\theta$ is defined by solving:

$$\left\langle \frac{\partial \mathcal{L}}{\partial \theta}, h \right\rangle = \left\langle \frac{\partial J^*}{\partial \theta}, h \right\rangle + \int_{\Omega} \left(\frac{\partial \sigma}{\partial \theta} : e(\underline{u}) + \left(\frac{\partial b}{\partial \theta} \nabla p \cdot \underline{u} + \frac{\partial K_D^*}{\partial \theta} \nabla \hat{p} \cdot \nabla \underline{\hat{p}} dx + \ell \right) h dx, \right. \quad (38)$$

where the descend direction $h = d\theta$ has to satisfy the inequality

$$\left\langle \frac{\partial \mathcal{L}}{\partial \theta}(\theta, u, \underline{u}, p, \underline{p}, \ell), d\theta \right\rangle < 0, \quad (39)$$

which is achieved by choosing

$$d\theta = - \left(\frac{\partial J_1^*}{\partial \theta}(\theta) + \frac{\partial \sigma}{\partial \theta} : e(\underline{u}) + \frac{\partial b}{\partial \theta} \nabla p \cdot \underline{u} + \frac{\partial K_D^*}{\partial \theta} \nabla \hat{p} \cdot \nabla \underline{\hat{p}} dx + \ell \right) \quad (40)$$

with $\langle \frac{\partial J^*}{\partial \theta}, h \rangle = \int_{\Omega} \frac{\partial J_1^*}{\partial \theta} \cdot h dx$. At iteration n , the optimal density θ is then updated by performing the projected gradient:

$$\theta^{n+1} = P_{[0,1]}(\theta^n + \delta d\theta), \quad (41)$$

where $\delta > 0$ is the step size and, in practice, we use an adaptive step size δ , i.e., at each iteration, if the newly computed composite structure is accepted (that is, if the current objective function $J^*(\theta^n)$ is lower than previous one $J^*(\theta^{n-1})$), the step size δ is increased of 20%, else if it is rejected, the step size is divided by 2. $P_{[0,1]}$ is the projection operator on the interval $[0, 1]$. Numerically, the partial derivative of the Lagrangian $\frac{\partial \mathcal{L}}{\partial \theta}$ is regularized using an equivalent H^1 -norm:

$$\begin{aligned} & \int_{\Omega} \left(\frac{\partial \mathcal{L}}{\partial \theta} h + \eta^2 \nabla \frac{\partial \mathcal{L}}{\partial \theta} \cdot \nabla h \right) dx = \left\langle \frac{\partial J^*}{\partial \theta}, h \right\rangle \\ & + \int_{\Omega} \left(\frac{\partial \sigma}{\partial \theta} : e(\underline{u}) + \frac{\partial b}{\partial \theta} \nabla p \cdot \underline{u} + \frac{\partial K_D^*}{\partial \theta} \nabla p \cdot \nabla \underline{p} + \ell \right) h dx, \end{aligned} \quad (42)$$

where η is a small coefficient, which typically depends on the size of the elements of the mesh: thanks to this coefficient, we are able to numerically regularize the partial derivative on a length scale of order η and to limit the checkerboard effect on the density θ . Note that, equation (42) is solved after solving the states equations (35)-(36), followed by the adjoint equations (33)-(34). We recall that, the solution h of Eq. (42) is the descend direction $h = d\theta$ satisfying Eq. (39); the effect of which is to update the optimal density θ by performing the projected gradient (41).

5.1.3 Complete optimization algorithm.

The alternate directions algorithm is an iterative method, structured as follows:

1. Initialization of the design variable θ such that :

$$\forall x \in \Omega, \quad \theta^0(x) = \frac{\Theta}{\int_{\Omega} 1 \, dx}$$

2. Iteration until convergence, for $n \geq 0$:

- (a) Computation of the state variable p^n through the Biot-Darcy model (24), with the design $(\theta^n, A^*(x))$
- (b) Computation of the stress tensor σ^n through the poro-linear elasticity problem (25), with the design shape $(\theta^n, A^*(x))$ and descend direction $d\theta^n$ for a given stress tensor σ^n using formulas (40)
- (c) Updating the design variable θ^{n+1} using formulas (41) for the descend direction $d\theta^n$ and then updating the design $(\theta^{n+1}, A^*(x))$, by linear interpolation.

6 Numerical results and discussion

We introduce our numerical results in the two physics context detailed in Section 3. A variety of 2-D test cases are presented to demonstrate that our alternate minimization algorithm produces physically correct results. The algorithm (5.1.3) has been implemented in FreeFem++ [34], where all the unknowns are discretized using P_1 finite elements and, the workspace Ω is discretized with triangular elements in 2-D. For all our computations, a linear material model with Young's modulus $\mathbf{E} = 12 \times 10^9 Nm^{-2}$ and Poisson's ratio $\nu = 0.35$ are considered. The void ($\theta = 0$) is replaced with a very compliant material: the smallest admissible value of θ is fixed at 10^{-4} , in order to avoid singularities of the effective tensor when the elasticity problem is solved.

We propose four test cases: first two are inspired from similar examples in [20, 21] and, the last two are new to the best of our knowledge. For the first three examples hereby, we aim to minimize the compliance of the solid body under pressure loads and volume constraint, that is:

$$J^*(\theta, u(\theta)) = \int_{\Omega} A^* e(u) : e(u) \, dx, \quad \text{such that} \quad \frac{1}{|\Omega|} \int_{\Omega} \theta \, dx = \Theta \quad (43)$$

6.1 Pressurized arch

This example was originally introduced and solved in [20, 21]; the bounding box of the structure is a rectangle of dimensions $L_x(m) \times L_y(m)$, fixed on the lower-left and lower-right edges, on a zone of width $\frac{L_y}{8}$, while submitted to a pressure load $p = 10^5 Nm^{-2}$ (bar) on its lower boundary Γ_p^f . For all other boundaries of this device, the pressure is null ($p = 0$) on $\Gamma_{p_0}^f$; see Fig.5 for a schematic of this test case.

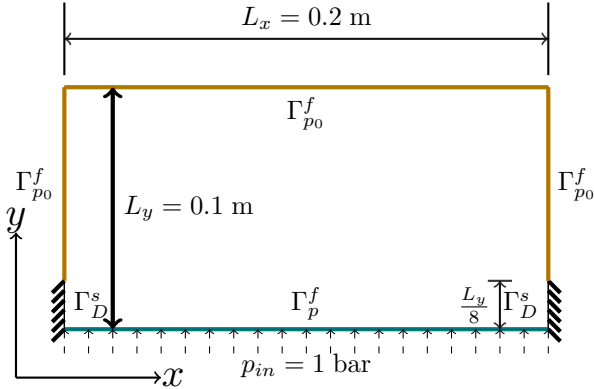


Fig. 5 Setting for the compliance minimization problem of 6.1 issued from [20, 21]

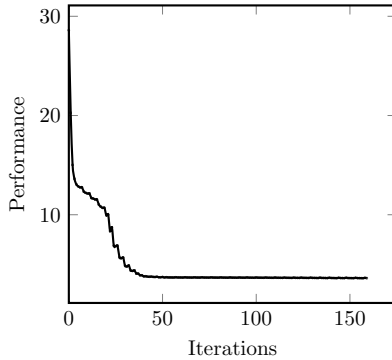


Fig. 6 Convergence history for the compliance minimization problem of Section 6.1

On Fig. 6, we plot the convergence history for the objective function (43): smooth and rapid convergence is observed. The output of the alternate minimization algorithm for a volume constraint set to $\Theta = 20\%$ of the total volume is displayed by Fig.7; the optimal density, pressure field, solid displacement and von Mises stress at the final state are depicted. For this latter, the density θ is represented with a gray scale: regions where $\theta = 1$ are black (pure material), whereas white regions correspond to voids and, the gray regions correspond to the homogenized material with microstructures (periodically perforated by hexagonal cells).

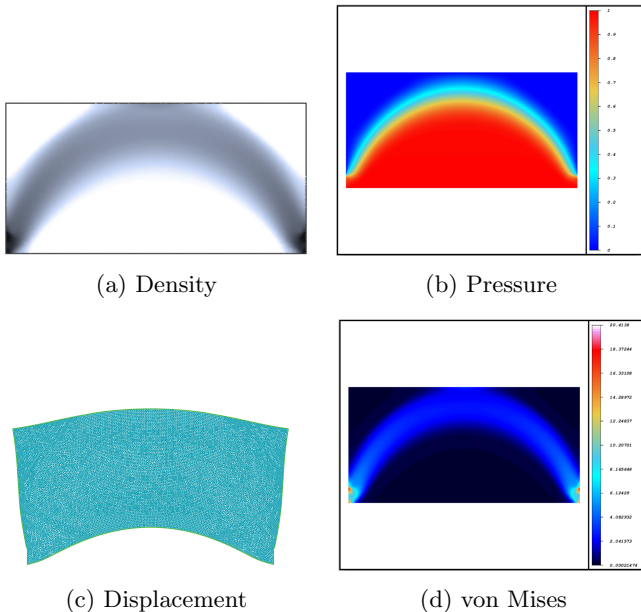


Fig. 7 (a) The optimal density, (b) pressure field p (bar), (c) displacement u , and (d) von Mises stress for test case 6.1

The topology of the result is similar to that obtained in previous literature [21], for similar problem but with different design (i.e., black and white design) and optimization setting (i.e., a density-based method). We note that, the algorithm tends to distribute more material in areas with high pressure gradients, of which one can clearly see a silhouette in the "shape" of an arch, although contains a large composite zone in its center. For the pressure field, we notice that the boundary conditions are respected: regions with high pressure gradients are located mainly on the arch and elsewhere, the pressure is diffuse.

6.2 Pressurized piston

This second example was originally introduced and solved in [21, 35]. The computational domain is a rectangle of dimensions $L_x(m) \times L_y(m)$, fixed on the left and right edges (in direction x) and on a small surface of its lower-middle wall (in both directions xy), while submitted to pressure load $p = 10^5 Nm^{-2}$ (bar) on the upper wall Γ_p^f . For all other boundaries of this device, the pressure is null; see Fig. 8 for a schematic of this test case. Again, our aim is to minimize the mechanical efforts induced in the solid structure by the stress imposed by the fluid, subjected to the volume constraint (43). For this calculation, the volume fraction is set to $\Theta = 30\%$.

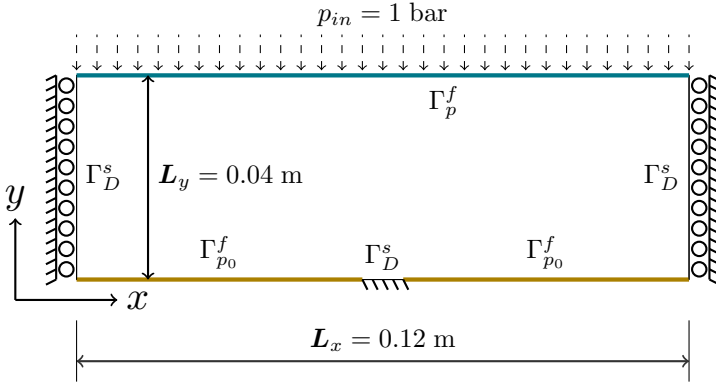


Fig. 8 Setting for the compliance minimization problem of 6.2 issued from [21, 35]

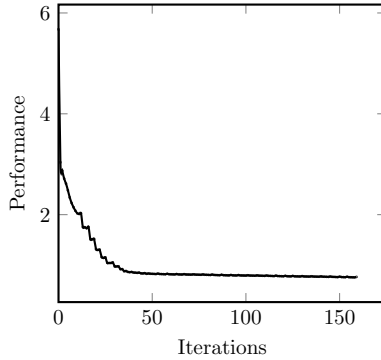


Fig. 9 Convergence history for the compliance minimization problem of Section 6.2

On Fig. 9, we plot the convergence history for this calculation: smooth and relatively rapid convergence is observed. For this latter, Fig. 10 displays the optimal density, pressure field, solid displacement and von Mises stress at final state. The topology of the result is similar to that obtained in previous literature [18, 21, 36, 37], for similar problems but with different design (i.e., a black and white design) and optimization settings (i.e., density-based methods). Again, we emphasize that, the algorithm tends to distribute more materials in areas with high pressure gradients, of which one can clearly see a silhouette in the "shape" of a piston, with a large composite zone at its center. For the pressure field, we note that the boundary conditions are respected: regions with high pressure gradients are located mainly on the piston and elsewhere, the pressure is diffuse.

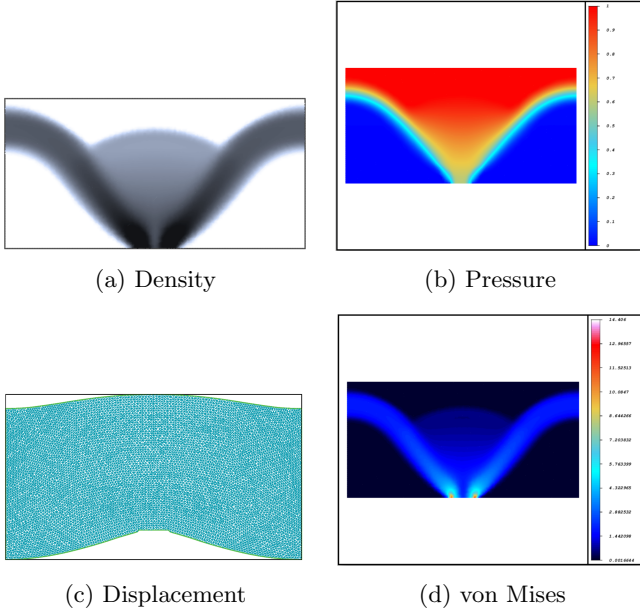


Fig. 10 (a) The optimal density, (b) pressure field p (bar), (c) displacement u , and (d) von Mises stress for test case 6.2

6.3 Pressurized MBB

Our third example is new, to the best of our knowledge. However, this test case is equivalent to very known pure-mechanical version in the literature, that is, the MBB-beam. The computational domain is a rectangle of dimensions $L_x(m) \times L_y(m)$, fixed on the left edge (in direction x) and on a small surface of its lower-right boundary (in direction y), while submitted to pressure load $p = 10^5 Nm^{-2}$ (bar) on a small part of its upper boundary Γ_p^f . On the lower boundary $\Gamma_{p_0}^f$, the pressure is null and the remaining boundaries are free of boundary conditions; see Fig. 11, for a schematic of this test case.

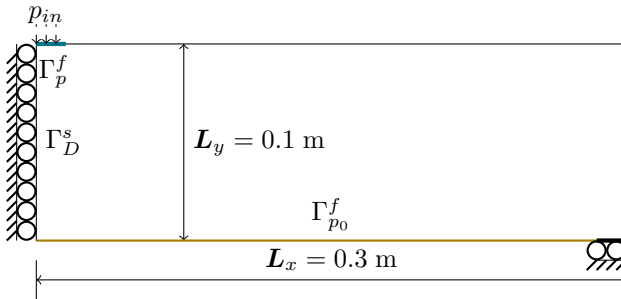


Fig. 11 Setting for the compliance minimization problem of Section 6.3

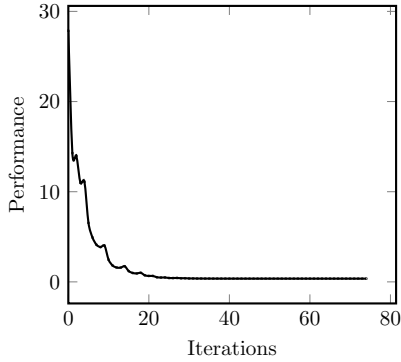


Fig. 12 Convergence history for the compliance minimization problem of Section 6.3

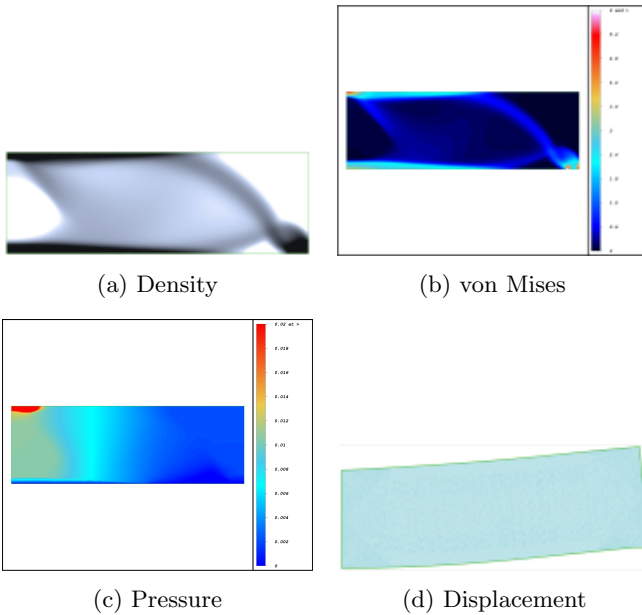


Fig. 13 The optimal density, (b) von Mises stress, (c) pressure field p (bar), and (d) displacement u for test case 6.3

Once again, our aim is to minimize the mechanical efforts (43) and, for this calculation, the volume fraction is set to $\Theta = 30\%$. On Fig. 12, we plot the convergence history for this calculation: smooth and relatively rapid convergence is observed. For this latter, Fig. 13 depicts the topology of the final design and the resulting von Mises stress, pressure field and solid displacement, under pressure loads at the final state. Very interestingly, we retrieve the fact that the topology of the result is similar to that obtained in the case

of pure-elastic, under mechanical load; see Fig 14, for the optimal MBB-beam design in pure-elastic case, wherein, the solution is autopenalized.

Once again, we note that, the algorithm tends to distribute more materials in areas with high pressure gradients, of which one can clearly see a silhouette in the "shape" of a beam, with a large composite zone at its center. For the pressure field, we note that, the boundary conditions are respected: regions with high pressure gradients are located mainly on the edges of the beam and elsewhere, the pressure is very diffuse. We emphasize that, for all the three examples above, similar topology optimization is observed for the design of the least compliant structure, under pressure loads and volume constraints: our alternate minimization algorithm tends to distribute more materials in areas with high pressure gradients, as we expected.



Fig. 14 The optimal design (autopenalized) in pure-elastic case, under mechanical load.

6.4 Two dimensional counter-flow exchanger

Finally, our last example, which is new to the best of our knowledge (although inspired from an example in the literature [38]). The computational domain is a two-dimensional counter-flow exchanger of dimensions $0.2(m) \times 0.22(m)$. A fluid of a density $\mathbf{q}_{0,1}$ (kgm^2s^{-1}) is entering at the lower-left part of the domain, with the corresponding pressure load on the opposite lower-right side, whereas a fluid of a density $\mathbf{q}_{0,2}$ (kgm^2s^{-1}) is also entering at the upper-right side of the domain, with the corresponding pressure load p_0 (bar) at the opposite upper-left side. All the other boundaries are insulated from the outside: zero Neumann boundary conditions hold for the pressure, while homogeneous Dirichlet boundary conditions are applied on the boundary of a small non optimizable rectangle ω of dimensions $0.2m \times 0.02m$; the setup is seen in Fig. 15. On Fig. 16, we displayed the numerical values of the parameters involved.

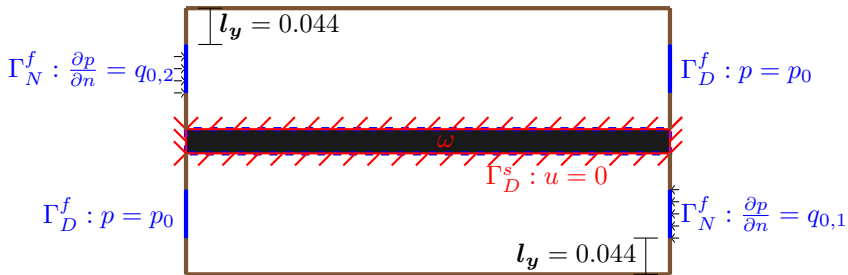


Fig. 15 Setting of the 2-D counter-flow exchanger of Section 6.4. The brown layers at the walls stand for zero Neumann boundary conditions for the pressure; homogeneous Dirichlet boundary conditions hold on $\partial\omega$.

p_0	$q_{0,1}$	$q_{0,2}$
1.5	3	5

Fig. 16 Numerical values of the physical parameters in the 2-D counter-flow exchanger 6.4

Here, we aim to achieve a trade-off between the minimization of the compliance (imposed by the fluid pressure) and the maximization of the hydraulic power (transmitted to the system), subject to a volume constraint, that is:

$$\begin{aligned}
 J^*(\theta, u(\theta)) = & \underbrace{\alpha \left(\int_{\Omega} A^* e(u) : e(u) \, dx \right)}_{\text{Elastic strain energy}} + (1 - \alpha) \underbrace{\left(\int_{\Omega} \mathbf{q} \cdot \nabla p \, dx \right)}_{\text{Hydraulic power}}, \\
 & s.t. \left\{ \frac{1}{|\Omega|} \int_{\Omega} \theta \, dx = \Theta \right.
 \end{aligned} \tag{44}$$

for some fixed coefficient $\alpha \in [0, 1]$: the relative weight given to each term in (44); wherein, $\mathbf{q} := -K^* \nabla p$, characterizes the flux (kgm^2s^{-1}). For this calculation, we consider two configurations: first, a test case with volume constraint set to $\Theta = 20\%$, second, a test case without volume constraint, for different values of α .

Fig. 17-18 display the optimal densities for some fixed values of α , in both configurations: with or without volume constraint. Very interestingly, we retrieve the fact that in the first configuration, the optimal distribution of the density is very diffuse in the case $\alpha < 0.5$, whereas, its becomes more dense in the case $\alpha \geq 0.5$. Consequently, the algorithm seems to be driven by the hydraulic power in the case $\alpha < 0.5$, then, by the elastic strain energy, in the case $\alpha \geq 0.5$. However, in the second configuration, the optimal distribution is very diffuse in general and becomes less diffuse for $\alpha \geq 0.5$: the algorithm seems to be driven by the hydraulic power.

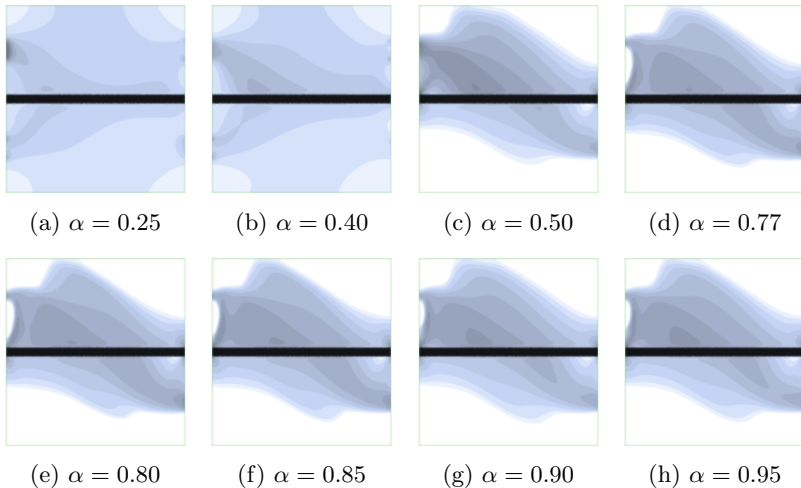


Fig. 17 Optimal densities for different values of α , with a given volume fraction $\Theta = 20\%$

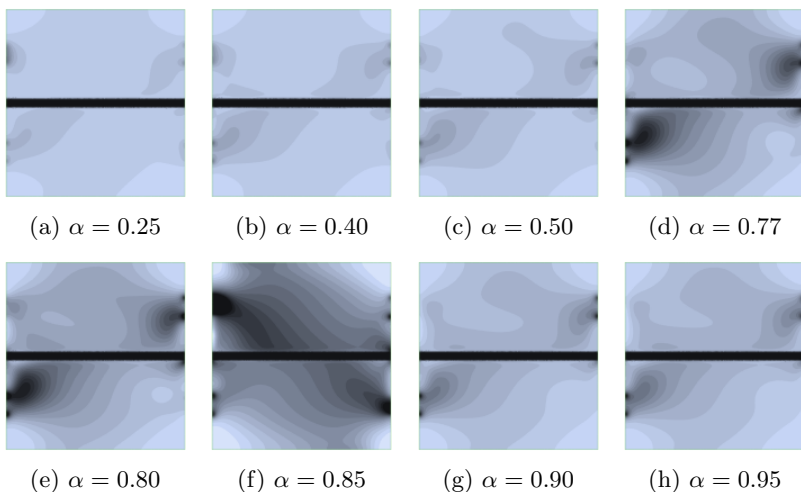


Fig. 18 Optimal densities for different values of α , without volume constraint

For the pressure field in both configurations, we notice that the boundary conditions are respected: regions with high pressure gradients are located mainly at the boundaries under fluid-pressure loads and elsewhere, its becomes very diffuse. We emphasize that, in both configurations, the topology of the result tends to achieve a trade-off between the minimization of the compliance (of the solid) induced by the fluid and the maximization of the hydraulic power, as we expected prior to our analysis. However, in the second configuration

(where volume is unconstrained), we note a gain of volume fraction but not necessarily a gain in performance; see Fig. 20 and Fig. 21.

α	0.25	0.40	0.50	0.77	0.85	0.90	0.93	0.95
$J^*(\alpha)$	-4.51	-0.06	0.962	5.055	5.025	6.533	10.17	0.163

Fig. 19 The converged objective function with respect to α , under the volume constraint $\Theta = 20\%$

α	0.25	0.40	0.50	0.77	0.85	0.90	0.93	0.95
$J^*(\alpha)$	-4.51	-2.54	-1.83	-0.57	-0.55	-1.47	0.026	0.286

Fig. 20 The converged objective function with respect to α , with no volume constraint

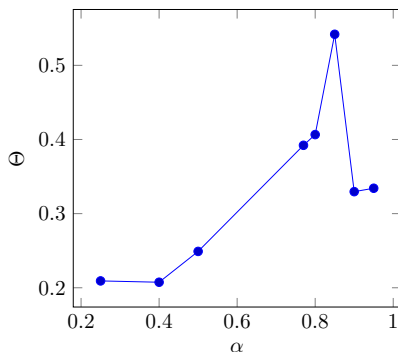


Fig. 21 The final volume history with respect to α , in the second configuration: no volume constraint.

The corresponding objective history, in both configurations are depicted on Fig. 19 and Fig. 20. On Fig. 21, we plot the final volume with respect to α , in the second situation, while on Fig. 22 and Fig. 23, we show the convergence history for $\alpha = 1/2$, in both configurations. On Fig. 24, we display the corresponding pressure field for both configurations, for $\alpha = 1/2$.

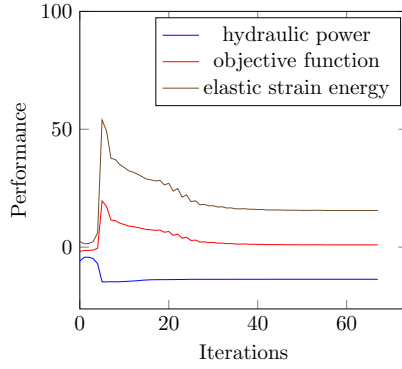


Fig. 22 The convergence history for $\alpha = 1/2$, under the volume constraint $\Theta = 20\%$

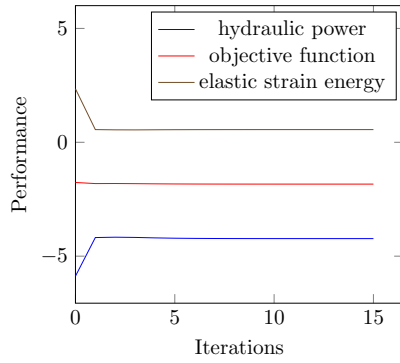


Fig. 23 The convergence history for $\alpha = 1/2$, without volume constraint

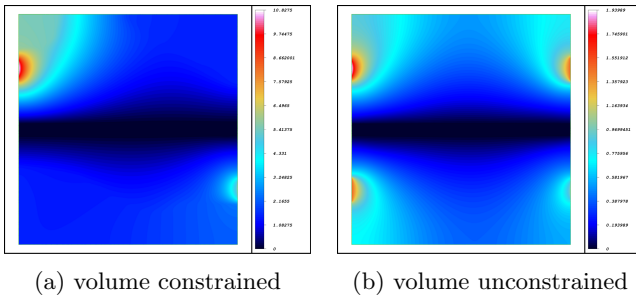


Fig. 24 The pressure field p (bar) at final state for both configuration: with and without volume constraint, for $\alpha = 1/2$

7 Conclusion and perspectives

In this study, we have demonstrated the relevance of shape and topology optimization for generating unconventional design problems involving two-physic interactions using the homogenization method. In our proposed method, Biot-Darcy's law is employed to characterize the pressure (of the fluid flow); the effect of which is to weakly couple to the solid phase by solving the associated PDEs using the standard finite element method. The porosity of each finite element is related to the material density through a smooth enough function to ensure a smooth transition between void and solid phases; the physical parameters are numerically computed in the case of isotropic porous medium. The method facilitates calculation of the load sensitivities with respect to the design variables, using the computationally inexpensive adjoint-state method [1, 9]; it is noticed that considerations of load sensitivities within the approach does alter the composite designs and are particularly important when designing multi-physic systems. In contrast to methods that use explicit boundary tracking, the Biot-Darcy's model offers the potential for relatively straightforward extension to 3-D problems. The effectiveness and robustness of the proposed homogenization method is verified by minimizing several arbitrary objective functionals.

Acknowledgments. This research project was fully sponsored by IFPEN: IFP énergies nouvelles.

Declarations

On behalf of all authors, the corresponding author states that there is no conflict of interest.

Replication of results

On behalf of all authors, the corresponding author states that there is no codes available as supplementary material because this work is carried out as part of a thesis in partnership with IFPEN. The latter holds the intellectual rights.

References

- [1] Allaire, G., Shape Optimization by the Homogenization Method, Springer, Applied Mathematical Sciences, 146 (2002).
- [2] Murat, F., Contre-exemples pour divers problèmes où le contrôle intervient dans les coefficients, *Ann. Mat. Pura Appl.*, 112 (1997) 49-68.
- [3] Kohn, R.V. and Strang, G., Optimal design and relaxation of variational problems, I. *Comm. Pure Appl. Math.*, 39(1) (1986) 113-137.
- [4] Lurie, K.A. and Cherkaev, A.V. and Fedorov, A.V., Regularization of optimal design problems for bars and plates, I, II. *J. Optim. Theory Appl.*, 37(4) (1982) 499-522, 523-543.
- [5] Bendsøe, M.P. and Kikuchi, N., Generating optimal topologies in structural design using a homogenization method, *Comput. Methods Appl. Mech. Engrg.*, 71(2) (1988) 197-224.
- [6] Bendsøe, M.P., Optimal shape design as a material distribution problem, *Structural and multidisciplinary optimization*, 1(4) (1989) 193-202.
- [7] Bendsøe, M.P. and Sigmund, O., *Topology optimization: theory, methods, and applications*, Springer Science & Business Media, (2003).
- [8] Allaire, G. and Geoffroy-Donders, P. and Pantz, O., Topology optimization of modulated and oriented periodic microstructures by the homogenization method, *Computers & Mathematics with Applications*, 78(7), (2019) 2197-2229.
- [9] Allaire, G., *Conception optimale de structures*, Springer Berlin, Heidelberg, (2007).

- [10] C ea, J., Conception optimale ou identification de formes, calcul rapide de la d eriv e directionnelle de la fonction co ˆut, *ESAIM: Mathematical Modelling and Numerical Analysis*, 30(6) (1986) 371-402.
- [11] Hammer, V.B. and Olhoff, N., Topology optimization of continuum structures subjected to pressure loading, *J. Structural and Multidisciplinary Optimization*, 19(2) (2000) 85-92.
- [12] Mendes, E. and Sivapuram, R. and Rodriguez, R. and Sampaio, M. and Picelli, R., Topology optimization for stability problems of submerged structures using the TOBS method, *Computers & Structures*, 259 (2022) 106-685.
- [13] Wang, C. and Zhao, M. and Ge, T., Structural topology optimization with design-dependent pressure loads, *Structural and Multidisciplinary Optimization*, 53(5):1005-1018 (2016).
- [14] Picelli, R. and Neofytou, A. and Kim, HA., Topology optimization for design-dependent hydrostatic pressure loading via the level-set method, *Structural and Multidisciplinary Optimization*, 60(4):1313-1326 (2019).
- [15] Feppon, F. and Allaire, G. and Bordeu, F. and Cortial, J. and Dapogny, C., Shape Optimization of a Coupled Thermal Fluid-Structure Problem in a Level Set Mesh Evolution Framework, *J. Boletín de la Sociedad Espa ˜nola de Matemática Aplicada*, Springer 76(3) (2019) 413-458.
- [16] Du, J. and Olhoff, N., Topological optimization of continuum structures with design-dependent surface loading - Part I: New computational approach for 2D problems, *J. Structural and Multidisciplinary Optimization* 27(3) (2004) 151-165.
- [17] Fuchs, M.B. and Shemesh, NNY., Density-based topological design of structures subjected to water pressure using a parametric loading surface, *J. Structural and Multidisciplinary Optimization*, 28(1) (2004) 11-19.
- [18] Lee, E. and Martins, JRRA., Structural topology optimization with design-dependent pressure loads, *J. Computer Methods in Applied Mechanics and Engineering*, 40-48 (2012) 233-236.
- [19] Li, Zm and Yu, J. and Yu, Y. and Xu, L., Topology optimization of pressure structures based on regional contour tracking technology, *J. Structural and Multidisciplinary Optimization*, 58(2) (2018) 687-700.
- [20] Zheng, B. and Chang, C.J. and Gea, H.C., Topology optimization with design-dependent pressure loading, *J. Structural and Multidisciplinary Optimization*, 38(6) (2009) 535-543.

- [21] Kumar, P. and Frouws, J.S. and Langelaar, M., Topology Optimization of Fluidic Pressure Loaded Structures and Compliant Mechanisms using the Darcy Method, Springer: Structural and Multidisciplinary Optimization, 61 (2020) 1637-1655.
- [22] Kumar, P., TOPress: a MATLAB implementation for topology optimization of structures subjected to design-dependent pressure loads, Springer: Structural and Multidisciplinary Optimization 66, 97 (2023).
- [23] Hübner, D. and Rohan, E. and Lukeš, V. and Stingl, M., Optimization of the porous material described by the Biot model, Elsevier, International Journal of Solids and Structures, 156-157 (2019) 216-233.
- [24] Murat, F. and Tartar, L., Calcul des variations et homogénéisation, Les lectures de l'homogénéisation : théorie et applications en physique, (Eyrolles, 1985) 319-369.
- [25] Pantz, O. and Trabelsi, K., A post-treatment of the homogenization method for shape optimization, SIAM Journal on Control and Optimization, 47(3) (2008) 1380–1398.
- [26] Geoffroy-Donders, P., Homogenization method for topology optimization of structures built with lattice materials, PhD thesis, Université Paris Saclay (COMUE), 2018.
- [27] Neuber, H., Theory of notch stresses: principles for exact calculation of strength with reference to structural form and material, USAEC Office of Technical Information, (1961) 4547.
- [28] Abad, K.M.E. and Khanoki, A.S. and Pasini, D.F., Fatigue design of lattice materials via computational mechanics: Application to lattices with smooth transitions in cell geometry, International Journal of Fatigue, 47 (2013) 126-136.
- [29] Vigdergauz, S., Energy-minimizing inclusions in a planar elastic structure with macroisotropy, Structural optimization, 17(2-3) (2013) 104-112.
- [30] Hashin, Z. and Shtrikman, S., A variational approach to the theory of the elastic behaviour of multiphase materials, Journal of the Mechanics and Physics of Solids, 11(2) (1963) 127-140.
- [31] Batchelor, G., An introduction to fluid dynamics, Cambridge university press, 2000.
- [32] Suzuki, K. and Kikuchi, N., A homogenization method for shape and topology optimization, Comp. Meth. Appl. Mech. Eng., 93 (1991) 291-318.

- [33] Allaire, G. and Kohn, R.V., Optimal design for minimum weight and compliance in plane stress using extremal microstructures, *Europ. J. Mech. A/Solids*, 12(6) (1993) 839-878.
- [34] Hecht, F., *J. Math. Anal. Appl.*, New development in freefem++, *J. Numerical Mathematics*, (2012).
- [35] Bourdin, B. and Chambolle, A., Design-dependent loads in topology optimization, *ESAIM: Control, Optimisation and Calculus of Variations.*, 9 (2003) 19-48.
- [36] Wang, C. and Zhao, M. and Ge, T., Structural topology optimization with design-dependent pressure loads., *J. Structural and Multidisciplinary Optimization*, 53(5) (2016) 1005-1018.
- [37] Picelli, R. and Neofytou, A. and Kim, H.A., Structural topology optimization with design-dependent pressure loads., *Topology optimization for design-dependent hydrostatic pressure loading via the level-set method*, 60(4) (2019) 1313-1326.
- [38] Feppon, F., *Optimisation topologique de systèmes mutiphysiques*, Hal, [archives-ouvertes.fr](https://hal.archives-ouvertes.fr) (2019, Thèse, École Polytechnique Université Paris Saclay).